

Synthesis and Electrochemical Characterization of Silica-Manganese Oxide with a Core-shell Structure and Various Oxidation States

Seong-Hyeon Ryu, Seung-Gi Hwang, Su-Ryeon Yun, Kwon-Koo Cho,[†] Ki-Won Kim,[†] and Kwang-Sun Ryu^{*}

Department of Chemistry, University of Ulsan, Ulsan 680-749, Korea. *E-mail: ryuks@ulsan.ac.kr

[†]i-Cube Center, ITRC for Energy Storage and Conversion, Gyeongsang National University, Jinju, Gyeongsangnamdo 660-701, Korea

Received April 2, 2011, Accepted June 28, 2011

Silica-manganese oxides with a core-shell structure were synthesized *via* precipitation of manganese oxides on the SiO₂ core while varying the concentration of a precipitation agent. Elemental analysis, crystalline property investigation, and morphology observations using low- and high-resolution electron microscopes were applied to the synthesized silica-manganese oxides with the core-shell structure. As the concentration of the precipitating agent increased, the manganese oxide shells around the SiO₂ core sequentially appeared as Mn₃O₄ particles, Mn₂O₃+Mn₃O₄ thin layers, and α -MnO₂ urchin-like phases. The prepared samples were assembled as electrodes in a supercapacitor with 0.1 M Na₂SO₄ electrolyte, and their electrochemical properties were examined using cyclic voltammetry and charge-discharge cycling. The maximum specific capacitance obtained was 197 F g⁻¹ for the SiO₂-MnO₂ electrode due to the higher electronic conductivity of the MnO₂ shell compared to those of the Mn₂O₃ and Mn₃O₄ phases.

Key Words : Silica-manganese oxide, Core-shell structure, Supercapacitor, Electrode, Oxidation state

Introduction

Supercapacitors (ultra capacitors or electrochemical capacitors) are used as back-up power supplies for real-time clock electronics and are also widely used in industrial applications. Supercapacitors are charge (or energy) storage devices which can withstand higher powers than batteries and that can deliver higher energies than conventional electrostatic or electrolytic capacitors. Supercapacitors can be used as auxiliary energy devices along with a primary power enhancement in short-pulse applications. Electrochemical supercapacitors are classified based upon the mechanism of charge storage. One example is the electrical double layer capacitor, in which the capacitance arises from charge separation at the electrode/electrolyte interface. Another example is a pseudocapacitor (or redoxcapacitor), in which capacitance arises from faradaic reactions which, for a variety of different reasons, exhibit capacitive behavior.¹⁻⁴

The most widely used materials for supercapacitors include carbon, conducting polymers, and transition metal oxides. In electrical double layer capacitor systems, carbon in the form of active carbon or carbon nanotubes is generally used as the electrode material. In pseudo- or redox supercapacitor systems, transition metal oxides (ruthenium oxide, nickel oxide, and manganese oxide) and conducting polymers (polyaniline or polypyrrole) are commonly used as the electrode materials.³ Among the different transition metal oxides, amorphous hydrous RuO₂ has a high specific capacitance (~760 F g⁻¹) due to solid-state pseudo-faradaic reactions.^{5,6} However, its high cost, low porosity, and rapid decrease in power density at high charge-discharge rates are among the disadvantages of using RuO₂·xH₂O in practical

supercapacitors.⁷ Therefore, manganese oxides have received much attention and interest due to their low cost, natural abundance, and environmentally benign properties.

Manganese oxide can be synthesized *via* thermal decomposition, co-precipitation, sol-gel processes, electrochemical deposition, solution-based chemical routes, and solid-state reactions.⁸⁻¹⁶ Changes in the synthesis parameters such as current density, temperature, reactant concentration, and pH result in different physical, chemical, and electrochemical properties of manganese oxide. The synthesis conditions determine the intrinsic properties of the manganese oxide produced. Previously reported manganese oxides demonstrated specific capacitances as high as 600 F g⁻¹ for thin films and 150-300 F g⁻¹ for powder-based electrodes within a potential window of 0.9-1.2 V in aqueous electrolytes containing KCl, K₂SO₄, NaCl, or Na₂SO₄.¹⁰⁻²⁰

On the other hand, a surface nanoparticle coating has been used with various materials to form core-shell morphologies, resulting in the formation of new composite materials that can be used in the areas of electrochemistry, magnetics, mechanics, thermal conduction, electro-optics, electronics, photonics, and catalysis.²¹⁻²⁸ Silica coated with other materials is a classic combination which is widely used in many fields. In fact, silica has many merits when used in core-shell structures. First, silica can be easily produced in a controlled manner with a spherical morphology on the nano to micron scale. When silica spheres are coated with electro-active material, a spherical core-shell electro-active material will be obtained. The size of the electro-active material can be controlled by the sizes of the silica cores. Secondly, the non-agglomerated particles, narrow size distribution, and spherical shape offer many sites for the reduction reactions of the

electro-active material.²⁹

In this study, we synthesized silica and silica-manganese oxides with core-shell structures *via* the stöber and precipitation methods. The phases of the manganese oxides produced on the shell were controlled through the use of chelating and precipitation agents, which changed the oxidation states of the manganese species. The resultant silica-manganese oxides with different oxidation states were compared in terms of their physical and electrochemical properties for use as the electrode material of supercapacitors.

Experimental

The uniform silica spheres were synthesized using the stöber method. The silica nanoparticles were prepared using ammonia as a catalyst in order to form spherical particles. A 100 mL solution of 0.2 M tetraethylortho silicate (Aldrich) and ethanol (Daejung) was stirred for 1 h. Another 100 ml solution consisting of 0.6 M NH₄OH (Daejung), 17 M deionized water, and ethanol was stirred for 1 h. The two solutions were mixed into one vessel and constantly stirred to obtain a colloid state. The silica colloid was centrifuged and washed with deionized water and ethanol to yield a Si(OH)₂ gel. The gel was then dried at 70 °C for 10 h to obtain silica nanoparticles.

The silica nanoparticles (1 g) were dispersed in deionized water *via* ultrasonication for 2 h. A 0.044 M MnSO₄·H₂O (Samchun Chem.) solution was dissolved in deionized water and added dropwise to the silica solution under stirring. A mixed aqueous solution of 0.088 M NH₄OH and NaOH as a precipitation agent (varied among 0, 0.022, and 0.088 M) was also added dropwise to the silica solution under stirring. The black precipitate was washed with deionized water and dried at 70 °C for 10 h. The dried powder as a silica-manganese oxide precursor was heated at a rate of 1.5 °C min⁻¹ to 300 °C, maintained for 3 h, and cooled naturally to room temperature.

The morphologies of the silica-manganese oxide powders obtained with core-shell structures were evaluated using a field emission scanning electron microscope (FE-SEM, JSM-6500F, Jeol) and a field emission transmission electron microscope (FE-TEM, JEM 2100F, Jeol). The weight ratios of the metal elements were evaluated using inductively coupled plasma emission spectroscopy (ICP, Iris Duo, Thermo Electron). The X-ray diffraction (XRD) patterns were measured using a X-ray diffractometer (Ultra-X, Rigaku, CuK_α radiation) at a step scan of 0.02° to identify the crystalline phases of the silica-manganese oxides powders with core-shell structures. Fourier transform infrared (FT-IR) spectra were also recorded using a FT-IR spectrometer (Varian 2000) in the wavenumber range of 400 to 4,000 cm⁻¹. For the FT-IR test, the solid samples were diluted in KBr pellets.

The supercapacitor electrode was prepared by mixing and drying a mixture of the silica-manganese oxide with a core-shell structure (75 wt %) as an active material, carbon black

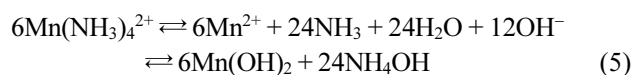
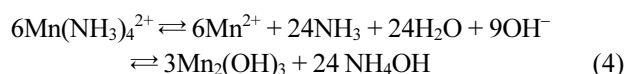
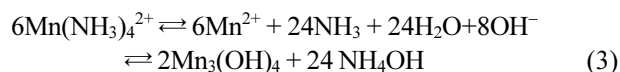
(20 wt %, Super P, Timcal Graphite & Carbon) as a conductive agent, poly(tetrafluoroethylene) (5 wt %, Aldrich) as a polymer binder, and 6 mL of ethanol in deionized water as a solvent. The dried mixture was converted to a rubber-like paste by pressing with isopropyl alcohol. The electrode, which was used as both the cathode and anode, was pressed onto a nickel-mesh current collector and surrounded with a separator. The supercapacitor cell was assembled by superimposing the cathode/separator/anode sheets with a 0.1 M Na₂SO₄ electrolyte and vacuum sealing within an aluminum pouch. For the supercapacitor cell, cyclic voltammetry (CV, WBCS3000, WonA Tech) was performed within the range of -0.2 to 1.0 V (*vs.* SCE) at a scan rate of 5 mV sec⁻¹. Galvanostatic charge-discharge cycling in the potential range of -0.2 V to 1.0 V was also performed at constant current densities of 0.1 and 0.2 A g⁻¹.

Results and Discussion

The precipitated silica nanoparticles have a three-dimensional network structure and contain silanol (Si-OH) groups on the surface. Silanol and siloxane groups are conventionally created on the silica surface, leading to the hydrophilic nature of the particles. Silica surfaces are typically classified into three silanol types: free or isolated silanols, hydrogen-bonded or vicinal silanols, and geminal silanols.³⁰ The manganese oxides can be synthesized through chelation and precipitation due to the manganese cations arranged around the silica nanoparticles. At this stage, the oxidation state of manganese oxide can be adjusted by varying conditions such as the alcohol, electrochemistry, and temperature.^{7,31,32} In the present work, the low reaction temperature slowly releases free Mn²⁺ cations from the stable precursor. These Mn²⁺ cations then form amine complexes of Mn(NH₃)_{*n*}²⁺ (*n*=1-4) with NH₃ (aq) in a moderately basic medium (e.g., pH=8). Due to the formation of amine complexes, the solution does not contain colloidal manganese hydroxide in the deposition solution. The chelation reaction can be expressed as follows.



In this work, the oxidation state of the manganese oxides is controlled by the concentration of the NaOH precipitation agent. The precipitation reactions are as follows.



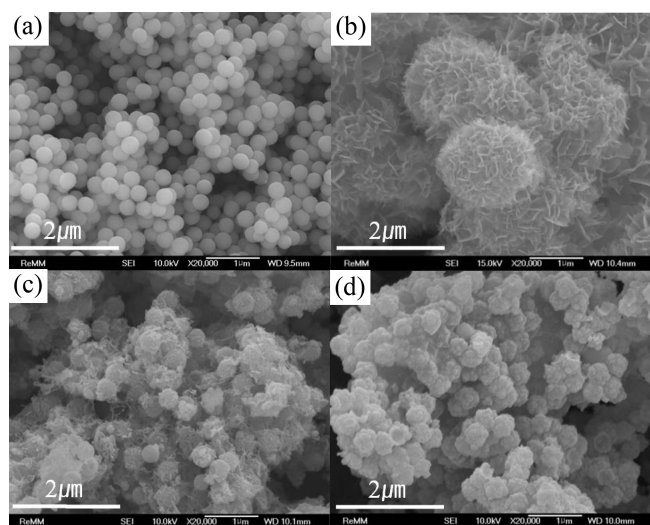
The hydroxide (OH) species are substituted with oxygen (O) species in the existence of NaOH to yield manganese oxides such as Mn₃O₄, Mn₂O₃, and MnO₂, as shown in Eqs. (3)-(5),

Table 1. ICP results and weight ratios of manganese oxide

Concentration of NaOH (M)	0.088	0.022	0
Weight of Si (mg kg ⁻¹)	162,000	220,300	154,900
Weight of Mn (mg kg ⁻¹)	366,000	327,200	329,100
Weight ratio of manganese oxide (%)	61.0	36.1	35.8

respectively. Thus, manganese oxide forms in the sequence of MnO₂, Mn₂O₃, and Mn₃O₄ phases as the concentration of NaOH increases. The phases of the manganese oxides may be related to the oxidation states of the Mn species. Table 1 shows the ICP results, which can be used to calculate the weight percentage of the manganese oxide. All samples are prepared using the same weight of manganese precursor and SiO₂. The oxidation state of the manganese ions increases from +2 to +4 as the content of the precipitation agent increases. The manganese oxide with a relatively high oxidation state has a higher weight percentage because the number of hydroxide ions per manganese ion increases with increasing manganese ion oxidation state.

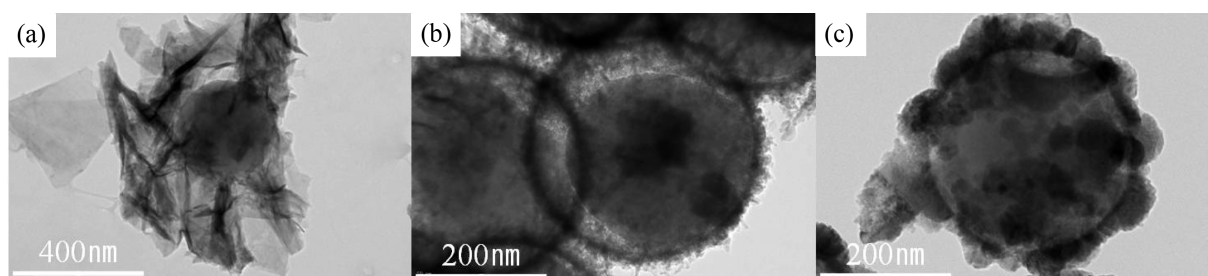
Figure 1 shows FE-SEM images of the silica-manganese oxides with a core-shell structure. In Figure 1(a), very uniformly distributed spheres with smooth surfaces are observed for the synthesized SiO₂ nanoparticles. For the powders


Figure 1. FE-SEM images of (a) pristine silica and silica-manganese oxides after the precipitation reaction at NaOH concentrations of (b) 0.088, (c) 0.022, and (d) 0.000 M.

obtained through the precipitation reaction (Figs. 1(b)-(d)), the obtained manganese oxides coated onto the surfaces of the SiO₂ nanoparticles are very uniform and spherical. In the absence of NaOH in the precipitation reaction (Fig. 1(b)), a urchin-like morphology is observed, which consists of plate-like manganese oxide species on the SiO₂ particles, as seen in the high-resolution image shown in Figure 2(a). At low and high concentrations of NaOH, rough surfaces on the SiO₂ core are observed with somewhat aggregated porous spherical particles, as seen in Figures 1(c) and 1(d). However, the FE-TEM images in Figures 2(b) and 2(c) confirm a mixture of thin layers and small particles on the surfaces of SiO₂ nanoparticles. Both the average diameter and the shell thickness for the powder without NaOH are higher than those of the other powders. This indicates that the NaOH precipitating agent plays a role in the distribution and dispersion of the shell species to yield a thin layered core-shell structure.

The XRD patterns of the obtained powders show the accurate chemical species of the shell, as shown in Figure 3. The pristine SiO₂ (Fig. 3(a)) shows a weak and broad peak in the range of 20-22.5°, corresponding to its amorphous nature. At a high concentration of NaOH precipitating agent (Fig. 3(b)), two main peaks (★) corresponding to the (311) and (440) planes of MnO₂ appear, which indicate poorly crystalline (space group *I4/m*) α-MnO₂ (JCPDS no. 42-1169).³¹ At a low concentration of NaOH (Fig. 3(c)), two types of peaks are simultaneously observed: a cubic phase (space group *La-3*) of Mn₂O₃ (JCPDS no. 41-1442) (■) and some planes of a normal tetragonal spinel structure (space group *I41/amd*) of hausmannite Mn₃O₄ (JCPDS no. 1-1127), indicating the coexistence of Mn₃O₄ and Mn₂O₃ phases. In the absence of NaOH (Fig. 3(d)), plane peaks (◆) of a normal tetragonal spinel structure (space group *I41/amd*) of hausmannite Mn₃O₄ (JCPDS 1-1127) are observed. In addition, it should be noted that all samples contain the same SiO₂ peak. Therefore, the shell regions of the obtained powder mainly consist of α-MnO₂, Mn₂O₃ + Mn₃O₄, and Mn₃O₄ as the concentration of NaOH decreases. Therefore, the core-shell species in the FE-SEM and FE-TEM images are identified as SiO₂-MnO₂ (Figs. 1(b) and 2(a)), SiO₂-Mn₂O₃+Mn₃O₄ (Figs. 1(c) and 2(b)), and SiO₂-Mn₃O₄ (Figs. 1(d) and 2(c)) as the concentration of NaOH decreases.

Figure 4 shows the FT-IR spectra of (a) pristine SiO₂ nanoparticles, (b) SiO₂-MnO₂, (c) SiO₂-Mn₂O₃+Mn₃O₄, and


Figure 2. FE-TEM images of silica-manganese oxides after the precipitation reaction at NaOH concentrations of (a) 0.088, (b) 0.022, and (c) 0.000 M.

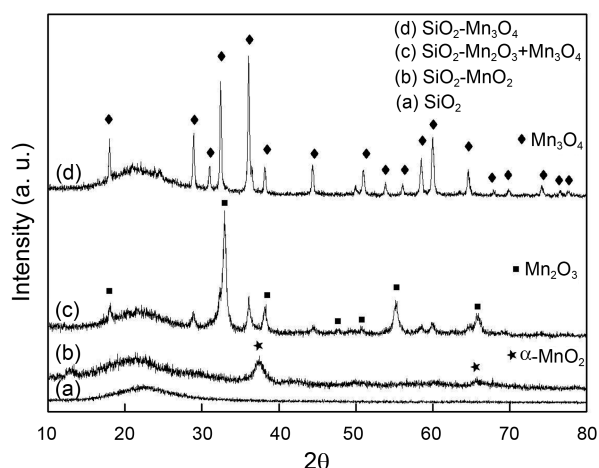


Figure 3. X-ray diffraction patterns of (a) pristine silica and silica-manganese oxides after the precipitation reaction at NaOH concentrations of (b) 0.088, (c) 0.022, and (d) 0.000 M. The (★), (■), and (◆) symbols correspond to the peaks of α - MnO_2 , Mn_2O_3 , and Mn_3O_4 , respectively.

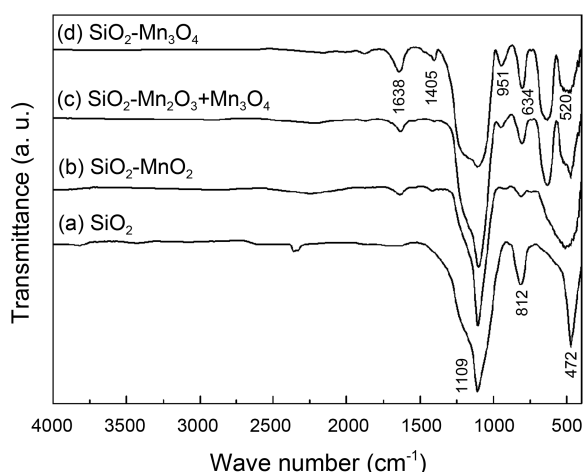


Figure 4. FT-IR spectra of silica-manganese oxides with a core-shell structure: (a) pristine SiO_2 , (b) SiO_2 - MnO_2 , (c) SiO_2 - Mn_2O_3 + Mn_3O_4 , and (d) SiO_2 - Mn_3O_4 .

(d) SiO_2 - Mn_3O_4 with core-shell structures. All spectra include equal bands related to SiO_2 such as the Si-O-Si asymmetric stretching vibration bands at about $1,100\text{ cm}^{-1}$, the Si-O-Si stretching vibration band at 812 cm^{-1} , and the bending vibration at 472 cm^{-1} . The bands at 1638, 1405, and 1110 cm^{-1} are normally attributed to O-H bending vibrations combined with Mn atoms, whereas the intense bands observed at 634 and 520 cm^{-1} are ascribed to the absorption of the Mn-O lattice vibrations in the tetragonally distorted cubic lattice.³³ These absorption peaks may be associated with the coupling mode between the Mn-O stretching modes of the tetrahedral and octahedral sites. This confirms the formation of the manganese oxide compound.

Combining the characterization results of the silica-manganese oxide powders with a core-shell structure, the formation mechanism shown in Figure 5 is suggested. The surface state of the silica particles after the addition of the

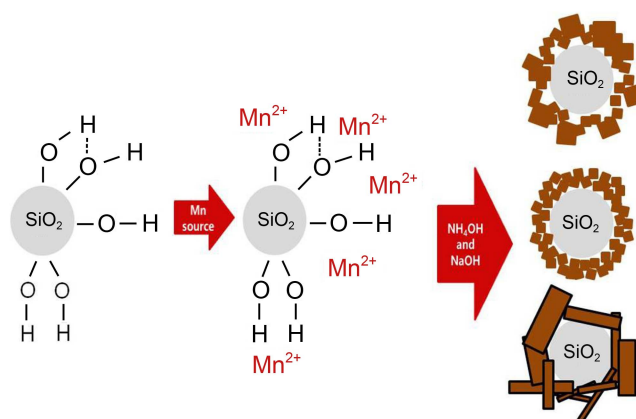


Figure 5. Schematic illustration of the formation mechanism of silica-manganese oxide with a core-shell structure.

Mn source can be ascribed to the dispersion of manganese cations, which yields amine complexes on the silica surfaces after addition of the chelating agent (NH_4OH). The thermal treatment in this equilibrium state between the amine complex and the chelating agent involves the aggregated Mn_3O_4 phase on the silica surface, according to Eq. (3). Next, the addition of the precipitating agent (NaOH) provides a high concentration of OH groups, which distributes and disperses the amine complexes to yield thin layer components of Mn_2O_3 and Mn_3O_4 phases on the silica surface, according to Eqs. (4) and (3), respectively. Further addition of NaOH results in a thick shell with a urchin-like structure on the silica surface to yield a MnO_2 phase, as shown in Eq. (5).

Manganese oxide as a shell component can be used as an active material of supercapacitors. Figure 6 shows the cyclic voltammograms for the silica-manganese oxides with a core-shell structure. The CV curves obtained in a 0.1 M of Na_2SO_4 solution at a sweep rate of 5 mV s^{-1} show a relatively rectangular mirror image with respect to the zero current line, indicating capacitive behavior. The SiO_2 - Mn_2O_3 + Mn_3O_4 and SiO_2 - MnO_2 show no redox peaks in the range of -0.2 V

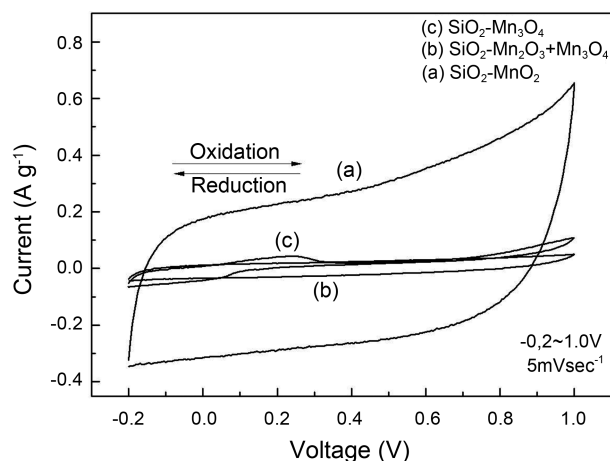


Figure 6. Cyclic voltammograms of silica-manganese oxides with a core-shell structure obtained at a scan rate of 5 mV s^{-1} : (a) SiO_2 - MnO_2 , (b) SiO_2 - Mn_2O_3 + Mn_3O_4 , and (c) SiO_2 - Mn_3O_4 .

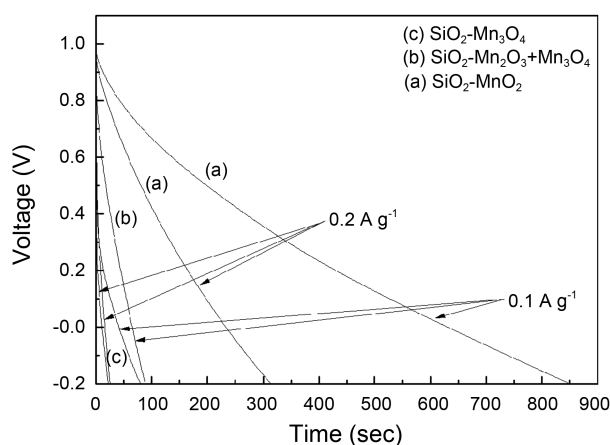


Figure 7. Discharge curves of silica-manganese oxides with a core-shell structure obtained at constant current densities of 0.1 and 0.2 A g^{-1} in the potential range of -0.2 V to 1.0 V: (a) $\text{SiO}_2\text{-MnO}_2$, (b) $\text{SiO}_2\text{-Mn}_2\text{O}_3\text{+Mn}_3\text{O}_4$, and (c) $\text{SiO}_2\text{-Mn}_3\text{O}_4$.

to 1.0 V, corresponding to ideal capacitive behavior. However, the $\text{SiO}_2\text{-Mn}_3\text{O}_4$ exhibits redox peaks near 0.2 V and 0.1 V, corresponding to the redox reaction between Mn^{2+} and Mn^{3+} . The specific capacitance (C_m) was calculated using the following equation,

$$C_m = \frac{i}{v}, \quad (6)$$

where V is the potential sweep rate (V sec^{-1}), i is the even current response defined by

$$i = \left(\int_{V_a}^{V_c} i(v)dv \right) / (V_c - V_a), \quad (7)$$

and V_a and V_c represent the lowest and highest voltages, respectively. The value of i is obtained by integrating the area of the CV curves. The specific capacitance values of $\text{SiO}_2\text{-Mn}_3\text{O}_4$, $\text{SiO}_2\text{-Mn}_2\text{O}_3\text{+Mn}_3\text{O}_4$, and $\text{SiO}_2\text{-MnO}_2$ obtained at a scan rate of 5 mV s^{-1} are 17 , 28 , and 197 F g^{-1} , respectively. The contribution of SiO_2 in the specific capacitance is excluded because SiO_2 can be considered as an inactive material of the supercapacitor. The $\text{SiO}_2\text{-MnO}_2$ case has a higher specific capacitance than does the MnO_2 obtained *via* the hydrothermal method.³⁴ The core-shell structure results in non-agglomerated manganese oxide with a narrow size distribution and a spherical shape. Also, the core-shell structure offers many reduction sites for the reduction of manganese oxide.

Figure 7 shows galvanostatic discharge curves obtained between -0.2 V to 1.0 V in a $0.1 \text{ M Na}_2\text{SO}_4$ solution at current densities of 0.1 and 0.2 A g^{-1} . The linear discharge curves indicate good capacitive behavior. The specific capacitance (C_m) was calculated using the following equation,

$$C_m = \frac{it}{\Delta v}, \quad (8)$$

where i is the current density (A), t is time (s), and Δv is the potential range (V). The specific capacitance values of $\text{SiO}_2\text{-Mn}_3\text{O}_4$, $\text{SiO}_2\text{-Mn}_2\text{O}_3\text{+Mn}_3\text{O}_4$, and $\text{SiO}_2\text{-MnO}_2$ at a current

density of 0.1 A g^{-1} are estimated to be 20 , 22 , and 117 F g^{-1} , respectively. The discharge of $\text{SiO}_2\text{-Mn}_3\text{O}_4$ begins at 0.5 V due to the iR decrease. In the specific capacitance results, the discharge curves are similar to the CV curves. This may be due to the different oxidation states ($2+$, $3+$, $4+$, and $6+$) of manganese oxide. The manganese oxides have electrochemical redox activity because the oxidation state of the manganese can vary from Mn^{4+} to Mn^{3+} and from Mn^{3+} to Mn^{2+} due to electron transfer. The Mn_2O_3 and Mn_3O_4 showed poor electronic conductivities. The MnO_2 easily participated in redox reactions because it has a higher oxidation state than those of Mn_2O_3 and Mn_3O_4 . Thus, The $\text{SiO}_2\text{-MnO}_2$ shows higher capacitance values than do $\text{SiO}_2\text{-Mn}_3\text{O}_4$ and $\text{SiO}_2\text{-Mn}_2\text{O}_3\text{+Mn}_3\text{O}_4$.

Conclusions

Silica-manganese oxides with core-shell structures were synthesized using a precipitation method. The XRD analysis clarified that the core regions of the composite particles is amorphous SiO_2 , and the shell region is a combination of poorly crystalline $\alpha\text{-MnO}_2$, a cubic phase of Mn_2O_3 , and a normal tetragonal spinel structure of Mn_3O_4 . The FT-IR spectra showed that the manganese oxide shell of the SiO_2 core gave rise to the presence of new bands at 520 , 634 , 1109 , 1405 , and 1638 cm^{-1} due to the bending vibrations of O-H, lattice vibrations of the Mn-O, and the stretching of Mn-O. The FE-SEM and FE-TEM images revealed that shells of Mn_3O_4 , Mn_2O_3 , and MnO_2 possess particles, thin layers, and a sea urchin shape with uniform particle sizes of 450 nm and 1 nm around the SiO_2 core. The synthesized Mn_3O_4 , Mn_2O_3 , and $\alpha\text{-MnO}_2$ in the core-shell structure were present at weight percentages of 35.8 , 36.1 , and 61.0% , respectively. The capacitances of $\text{SiO}_2\text{-Mn}_3\text{O}_4$, $\text{SiO}_2\text{-Mn}_2\text{O}_3\text{+Mn}_3\text{O}_4$, and $\text{SiO}_2\text{-MnO}_2$ were 17 , 28 , and 197 F g^{-1} , respectively. $\text{SiO}_2\text{-MnO}_2$ demonstrated a higher capacitance than did $\text{SiO}_2\text{-Mn}_3\text{O}_4$ and $\text{SiO}_2\text{-Mn}_2\text{O}_3\text{+Mn}_3\text{O}_4$.

Acknowledgments. This work was supported by the Mid-career Researcher Program through an NRF grant funded by the MEST (No. 2009-0093818) and by the development program of the local science park funded by the ULSAN Metropolitan City and the MEST (Ministry of Education, Science and Technology).

References

- Conway, B. E. *Electrochemical Supercapacitor-Scientific Fundamentals and Technological Application*; Kluwer Academic: New York, 1999; pp 29-31.
- Conway, B. E. *J. Electrochem. Soc.* **1991**, *138*, 1539.
- Sarangapani, S.; Tilak, B. V.; Chen, C. P. *J. Electrochem. Soc.* **1996**, *143*, 3791.
- Burke, A. *J. Power Sources* **2000**, *91*, 37.
- Zheng, J. P.; Jow, T. R. *J. Electrochem. Soc.* **1995**, *142*, L6.
- Zheng, J. P.; Cygan, P. J.; Jow, T. R. *J. Electrochem. Soc.* **1995**, *142*, 2699.
- Devaraj, S.; Munichandraiah, N. *J. Electrochem. Soc.* **2007**, *154*, A80.

8. Lee, H. Y.; Manivannan, A.; Goodenough, J. B. *C R Acad Sci.* **1999**, *200*, 565.
 9. Lee, H. Y.; Goodenough, J. B. *J. Solid State Chem.* **1999**, *144*, 220.
 10. Pang, S. C.; Anderson, M. A.; Chapman, T. W. *J. Electrochem. Soc.* **2000**, *147*, 444.
 11. Pang, S. C.; Anderson, M. A. *J. Mater Res.* **2000**, *15*, 2096.
 12. Chin, S. F.; Pang, S. C.; Anderson, M. A. *J. Electrochem. Soc.* **2002**, *149*, A379.
 13. Hu, C. C.; Tsou, T. W. *Electrochem. Commun.* **2002**, *4*, 105.
 14. Chang, J. K.; Tsai, W. T. *J. Electrochem. Soc.* **2003**, *150*, A1333.
 15. Ye, C.; Lin, Z. M.; Hui, S. Z. *J. Electrochem. Soc.* **2005**, *152*, A1272.
 16. Yuan, A.; Zhang, Q. *Electrochem. Commun.* **2006**, *8*, 1173.
 17. Jeong, Y. U.; Manthiram, A. *J. Electrochem. Soc.* **2002**, *149*, A379.
 18. Toupin, M.; Brousse, T.; Belange, D. *Chem. Mater.* **2004**, *16*, 3184.
 19. Prasad, K. R.; Miura, N. *J. Power Sources* **2004**, *135*, 354.
 20. Liu, E.-H.; Ding, R.; Meng, X.-Y.; Tan, S.-T.; Zhou, J. *J. Mater. Sci.: Mater Electron* **2007**, *18*, 1179.
 21. Caruso, R. A.; Antonietti, M. *Chem. Mater.* **2001**, *13*, 3272.
 22. Caruso, F.; Spasova, M.; Salgueirino-Maceira, V.; Liz-Marzán, L. M. *Adv. Mater.* **2001**, *13*, 1090.
 23. Jiang, Z. H.; Liu, C. Y. *J. Phys. Chem. B* **2003**, *107*, 12411.
 24. Sertchook, H.; Avnir, D. *Chem. Mater.* **2003**, *15*, 1690.
 25. Mulvaney, P.; Giersig, M.; Ung, T.; Liz-Marzán, L. M. *Adv. Mater.* **1997**, *9*, 570.
 26. Ung, T.; Liz-Marzán, L. M.; Mulvaney, P. *Langmuir* **1998**, *14*, 3740.
 27. Oldenburg, S. J.; Averitt, R. D.; Westcott, S. L.; Halas, N. J. *Chem. Phys. Lett.* **1998**, *288*, 243.
 28. Fleming, M. S.; Mandal, T. K.; Walt, D. R. *Chem. Mater.* **2001**, *13*, 2210.
 29. Lia, G.; Wanga, Z.; Yua, M.; Quana, Z.; Lin, J. *J. Solid State Chem.* **2006**, *179*, 2698.
 30. Zou, H.; Wu, S.; Shen, J. *Chem. Rev.* **2008**, *108*, 3893.
 31. Subramanian, V.; Zhu, H.; Wei, B. *Chem. Phys. Lett.* **2008**, *453*, 242.
 32. Shinomiya, T.; Gupta, V.; Miura, N. *Electrochim. Acta* **2006**, *51*, 4412.
 33. Julien, C. M.; Massot, M.; Poinignon, C. *Spectrochim. Acta* **2004**, *60*, 689.
 34. Subramanian, V.; Zhu, H.; Wei, B. *J. Power Sources* **2006**, *159*, 361.
-